ACS MATERIALS LETTERS

www.acsmaterialsletters.org Letter

Quantifying the Kinetics of UiO-66 Metal–Organic Framework Crystallization from X-ray Attenuation in the Zr K-Edge Region

Mikalai A. Artsiusheuski, Adam H. Clark, Maarten Nachtegaal, Nicola P. M. Casati, Jeroen A. van Bokhoven, and Vitaly L. Sushkevich*

Cite This: *ACS Materials Lett.* 2026, 8, 1974–1981 Read Online

ACCESS | Metrics & More | Article Recommendations | Supporting Information

ABSTRACT: X-ray absorption spectroscopy (XAS) provides element-specific information on local structures but is rarely used to follow macroscopic phase transformations. Here, we show that non-normalized transmission XAS spectra can be used to track phase-change kinetics in systems undergoing a single density-changing transformation. Using crystallization of the UiO-66 metal–organic framework (MOF) consisting of $[Zr_6O_4(OH)_4]^{12+}$ oxo-clusters as nodes and terephthalate linkers as a representative example, we demonstrate that changes in X-ray attenuation in Zr K-edge XAS spectra quantitatively mirror the evolution of crystalline material measured independently by in situ X-ray diffraction (XRD), enabling determination of the extent of solid formation without diffraction measurements. Kinetic analysis based solely on non-normalized X-ray attenuation yields a nucleation-growth mechanism identical to that obtained from multivariate curve resolution-alternating least squares (MCR-ALS) analysis of the full XAS dataset. Both approaches are consistent with the Gualtieri model of crystal formation and give identical activation energies for nucleation (80 ± 7 kJ mol^{-1}) and crystal growth (64 ± 5 kJ mol^{-1}). This approach links atomic-scale changes with macroscopic phase evolution and extends XAS to real-time monitoring of density-changing processes, including crystallization.

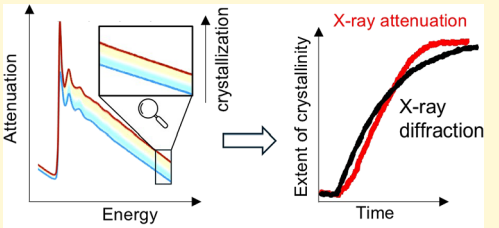

Non-normalized X-ray attenuation is equivalent to X-ray diffraction

1. INTRODUCTION

The synthesis of solid materials proceeds through complex sequences of chemical and structural transformations that dictate the resulting composition, morphology, and functional properties.[1,2] During nucleation and crystal growth, atomic or molecular precursors condense and reorganize into extended frameworks, establishing both local coordination environments and long-range periodicity.[3,4] The kinetics and mechanisms of these transformations determine crystal size, defect density, and distribution of active sites in different materials, including zeolites,[5] metal–organic frameworks,[6−8] quantum dots,[9] and metal halide perovskites,[6] thereby controlling their catalytic, sorption or electronic properties. However, the intermediate stages of synthesis, which are the subject of extensive investigation, vary across material systems and often involve the formation of soluble or amorphous species that are transient, disordered, and highly sensitive to the reaction environment, making their direct observation challenging.[3,10] Elucidating the mechanistic relationship between local chemical rearrangements and the onset of crystallization requires time-resolved methods capable of simultaneously probing short- and long-range order under realistic synthesis conditions.[11−13]

X-ray diffraction (XRD) remains the principal method for investigating crystallization phenomena because it directly probes long-range order and provides quantitative information on phase composition and crystallite size. Time-resolved in situ XRD studies reveal nucleation and growth kinetics across diverse systems, such as zeolites,[14] metal oxides,[15,16] and metal–organic frameworks (MOFs).[17,18] Yet, the XRD technique is inherently insensitive to local atomic and electronic environments, and when crystalline domains are nanometric or poorly ordered, diffraction peaks broaden and weaken, obscuring early-stage events and making it difficult to correlate emerging long-range order with concurrent chemical transformations. Moreover, XRD alone cannot resolve changes in oxidation state and coordination geometry that often precede nucleation.[19,20] Complementary techniques, such as Fourier-transform infrared spectroscopy (FTIR)[21,22] and Raman spectroscopy,[23] are widely used to probe MOF synthesis, particularly at early stages. Equally, a combination of XRD and differential scanning calorimetry (DSC) can be used to characterize the final MOF product.[24] However, these methods are not element-specific and often require acquisition conditions that differ from those of synthesis, limiting their applicability for true

Received: March 10, 2026
Revised: April 22, 2026
Accepted: May 8, 2026
Published: May 26, 2026

in situ measurements and direct correlation with crystallization processes.

X-ray absorption spectroscopy (XAS) complements XRD by probing the local atomic and electronic environment around specific elements without requiring periodicity and under synthesis-relevant conditions. The near-edge region (XANES) provides information on oxidation state and coordination symmetry,[25] while the extended region (EXAFS) yields quantitative metrics of interatomic distances and coordination numbers within the first and sometimes higher coordination shells.[26,27] These capabilities make XAS particularly valuable for tracking changes in element speciation, bond lengths, and oxidation states during nucleation and early growth.[28] However, because XAS is inherently local in nature, it cannot directly quantify long-range ordering and macroscopic crystallinity.

The complementarity of XRD and XAS has motivated numerous efforts to acquire both datasets under identical conditions[29,30] because it enables correlative analysis of chemical and structural evolution. However, the two methods require distinct photon-energy configurations: XRD typically employs a fixed high energy for scattering, whereas XAS acquisition involves continuous monochromator motion across a wide energy range near the X-ray absorption edge of the element of interest, and therefore, true simultaneous measurements with resolution in time domain of seconds is available only at specialized synchrotron beamlines.[31−35]

These limitations have motivated the development of strategies that extract both chemical and structural information from a single experimental technique. In transmission XAS, the X-ray absorption is proportional to the number of atoms in the X-ray beam path, weighted by their attenuation coefficients.[36] Away from the absorption edge, these coefficients vary only weakly with energy, and changes in the transmitted intensity therefore primarily reflect variations in the amount of condensed matter within the beam spot, rather than changes in electronic structure.[36] As a result, X-ray absorption can sensitively probe phase transformations that alter the number of atoms in the beam path. Related concepts have previously been used to follow the crystallization of barium titanate.[37] Recently, Lomachenko et al. proposed quantifying adsorbed species by monitoring absorption changes in the non-resonant X-ray attenuation in the pre-edge region of XAS spectra.[38] The desorption of water from solid material decreases number of atoms in the beam path and therefore leads to decrease in X-ray absorption.

Here, we introduce an approach that exploits the X-ray attenuation data extracted directly from non-normalized XAS to monitor macroscopic phase transformations (specifically, crystallization from true solution). When X-ray attenuation is dominated by X-ray absorption and contributions from elastic scattering are minor, temporal variations in the measured X-ray attenuation are proportional to the volumetric fractions of atoms in the beam path, which are, in turn, reflected by the amount of newly formed phase in the case of a single phase transformation. Measurements performed under resonant absorption conditions increase the relative contribution of absorption compared to elastic scattering, thereby strengthening the proportionality between X-ray attenuation and phase fraction. This allows to construct a time-resolved metric that tracks the progress of the phase transformation from a single transmission or fluorescence XAS measurement. While demonstrated here for the crystallization of the Zr-based metal–organic framework, the method is general and does not require the emerging phase to be crystalline; any transformation involving a density contrast between phases, such as amorphous condensation, gelation, or solid-state conversion, would produce a comparable change in X-ray attenuation provided absorption effects dominate over elastic scattering. This strategy bridges the gap between local and long-range probes without requiring reference standards, structural models, or separate diffraction experiments. The method allows for a simultaneous monitoring of the evolution of local coordination and long-range order to establish a versatile, accessible approach for in situ studies of nucleation and growth.

2. MATERIALS AND METHODS

2.1. Synthesis of Material

UiO-66 was synthesized from solutions prepared by dissolving 0.750 g of anhydrous zirconium chloride (Sigma Aldrich, 99%, freshly opened bottle) and 0.738 g of terephthalic acid (Sigma Aldrich, 99%) in 90 mL of *N*,*N*-dimethylformamide (DMF). 3.0 mL of 37 wt % aqueous hydrochloric acid (Merck, 99.5%) was added as a modulator for synthesis.

2.2. Zr K-Edge X-ray Absorption Spectroscopy (XAS)

Zirconium K-edge X-ray absorption spectroscopy (XAS) measurements were performed at the SuperXAS beamline of the Swiss Light Source (Switzerland).[39] The polychromatic X-ray beam was collimated using a rhodium-coated mirror to suppress higher-order harmonics, and subsequently monochromatized using a Si(111) channel-cut monochromator operating in quick-XAS mode at a frequency of 1 Hz. An energy range of 17800 to 19200 eV was selected to record the Zr K-edge XAS spectra. The monochromatic beam was focused to a spot size of 1500 × 400 μm using a toroidal rhodium-coated mirror. Spectra were acquired in transmission mode using 15 cm long ionization chamber detectors filled with a 1:1 N_2:Ar gas mixture at 2 bar. Simultaneously, a reference spectrum of zirconium metal foil was collected for energy calibration.

In situ XAS spectra during crystallization were acquired using a custom-designed cell installed between the first and second ionization chambers and operated via remote control (Scheme S1). For each experiment, the synthetic mixture was loaded into a soda lime glass capillary (2.0 mm outer diameter, 10 μm wall thickness, ∼70 mm length) and sealed using a propane/oxygen flame. The in situ cell was equipped with integrated heating elements, a Cr/Al thermocouple for temperature control, and a manual goniometer head (Huber) for precise alignment of the capillary in the X-ray beam. To compensate for heterogeneity in the reaction mixture, the capillary was continuously spun during the experiment. Following alignment, spinning was initiated, and the temperature was ramped to the target value at a rate of 10 K·min^{-1} while time-resolved XAS spectra were recorded. Data acquisition was terminated once the spectra stabilized, indicating completion of the crystallization process.

The acquired XAS spectra were averaged to increase the signal-to-noise ratio using the ProXAS software (60 spectra were averaged).[40] The evolution of X-ray attenuation as a function of time was quantified using metrics extracted from different spectral regions, including the pre-edge, post-edge, and edge-step at E_0. Average absorbance values were calculated within defined pre-edge (17750−17850 eV) and post-edge (18800−19000 eV) windows, while the edge-step was determined from the difference between fitted post-edge and pre-edge baselines at E_0 = 17998 keV. Pre-edge baselines were fit with a linear function, and post-edge baselines were described by an $A + BE^{-3}$ dependence. Multivariate analysis of the normalized time-resolved XAS data by multivariate curve resolution with alternating least squares (MCR-ALS) was carried out using ProXAS software.[34] The analysis was carried out under non-negativity constraints applied to time-dependent concentration profiles, and with the additional constraint,

https://doi.org/10.1021/acsmaterialslett.6c00237
ACS Materials Lett. 2026, 8, 1974−1981

the sum of component concentrations at each time point was equal to unity.

2.3. X-ray Diffraction (XRD)

Time-resolved X-ray diffraction (XRD) measurements were performed at the Materials Science beamline of the Swiss Light Source (Switzerland) using 25.2 keV radiation.[41,42] The in situ cell and sample preparation protocols were identical to those described in the XAS section. Diffraction patterns were recorded using a PILATUS 6 M detector positioned 1.00 m from the capillary. After beam focusing and alignment, the capillary was set to rotate continuously and heated to the target temperature at a rate of 10 K·min^{-1}. Upon reaching the desired temperature, time-resolved XRD patterns were collected approximately every 2 min until crystallization of UiO-66 was complete. The evolution of crystallinity as a function of time was quantified from XRD data by integrating the area under the characteristic Bragg peaks and normalizing the resulting intensity with respect to its maximum value. For fitting the crystallization curves using the Gualtieri model (vide infra), the nucleation parameter 'n' was fixed at 1.5, in accordance with previous reports.[19,20]

3. RESULTS AND DISCUSSION

Figure 1A,B shows the evolution of normalized Zr K-edge X-ray absorption near edge spectra (XANES) and Fourier transform (FT) of Extended X-ray Absorption Fine structure (EXAFS) spectra, respectively, during the synthesis of UiO-66. The synthetic solution initially contains dissolved zirconium chloride complexes, which are first converted into zirconium aqua species and subsequently transformed into $[Zr_6O_4(OH)_4]$ clusters − identical in structure to the secondary building units (SBUs) in the UiO-66 structure. These nodes then coordinate with terephthalic acid to assemble the final UiO-66 MOF structure.[19,20] The changes observed in the normalized Zr K-edge XANES and EXAFS spectra reflect the progressive evolution of the local coordination environment around Zr atoms.

Beyond changes in local coordination geometry reflected in the normalized XANES and EXAFS spectra, the absolute attenuation of the X-ray beam also evolves during crystallization. The measured X-ray attenuation contains contributions from absorption and elastic scattering. Absorption arises from interactions of the X-ray beam with individual atoms[36] and, for a fixed length path in a multiphase system, follow a linear mixing rule with respect to volumetric phase fractions (Section S2.1 of the Supporting Information). In contrast, elastic X-ray scattering includes coherent Bragg diffraction and small-angle scattering, both of which depend on crystallite size, long-range order, and electron density contras; these effects do not scale linearly with phase fractions.[43]

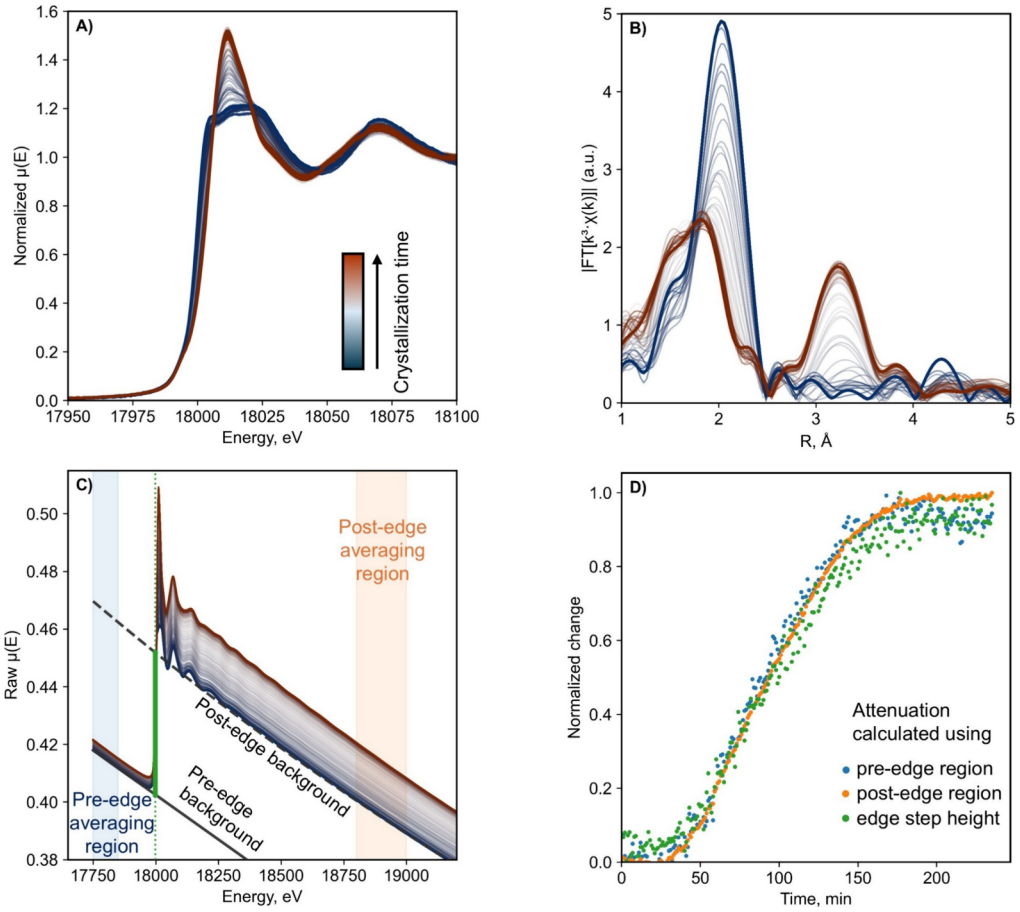

Figure 1. Zr K-edge X-ray absorption spectroscopy data obtained during UiO-66 synthesis at 363 K: (A) normalized Zr K-edge XANES spectra, (B) magnitude of the Fourier-transformed k^3-weighted EXAFS spectra (the Fourier transform was performed over a *k*-range of 3−15 Å^{-1}), (C) non-normalized Zr K-edge absorption spectra illustrating the pre-edge and post-edge background definitions, averaging windows, and the edge step evaluated at E_0, and (D) temporal evolution of relative pre-edge average attenuation (blue), post-edge average attenuation (orange), and edge step height (green).

https://doi.org/10.1021/acsmaterialslett.6c00237
ACS Materials Lett. 2026, 8, 1974−1981

Figure 1C show the evolution of the non-normalized attenuation during UiO-66 synthesis at 363 K (data for 353 and 373 K are shown in Figure S2, Supporting Information). In the pre-edge region, attenuation reflects non-resonant absorption from all constituent elements together with elastic scattering losses. Since both contributions may be comparable in magnitude, the relative influence of scattering cannot be a priori excluded. At energies above the absorption edge, however, the resonant Zr absorption increases sharply, amplifying the absorption term relative to pre-edge value and relative to elastic scattering, which typically varies smoothly with photon energy within this range. Due to resonant absorption, the post-edge region exhibits a larger absolute attenuation and improved signal to noise ratio for detecting changes in Zr density.

Another metric is obtained from the absorption edge step, evaluated at the edge energy by extrapolating smooth baselines fitted to the total attenuation on either side of the edge (Figure 1C, derivation in Section S2.1.4 of the Supporting Information). Since elastic-scattering contributions vary smoothly across the narrow energy interval spanning the edge, they largely cancel out in the step height, leaving predominantly the resonant discontinuity associated with Zr absorption. Consequently, the edge step is directly proportional to the volumetric Zr atomic density within the probed region.

Figure 1D shows the evolution of the normalized changes evaluated from attenuation in the pre-edge region, post-edge region, and absorption edge step, all calculated using eq 1, versus crystallization time. All metrics exhibit similar behavior suggesting that elastic scattering contributions are small under the present conditions and that attenuation changes are dominated by absorption. Notably, the attenuation changes from post-edge region displays much higher signal to noise ratio compared to the pre-edge metric, presumably due to much more effective resonant absorption compared to non-resonant one. Given the fixed probed volume and major contribution of absorption to the total attenuation, the normalized absorption change therefore provides a direct measure of crystallinity (for detailed derivation, refer to Section S2.1 in the Supporting Information):

$$\frac{M(t)-M(0)}{M(t_f)-M(0)}=\alpha(t) \quad (1)$$

where $M(t)$ represents the attenuation average in pre-edge or post-edge regions or the edge step height and $\alpha(t)$ is the volumetric fraction of crystalline UiO-66 relative to sample after complete crystallization. The smoother evolution of the post-edge signal is consistent with Zr resonant absorption being the dominant attenuation mechanism in this region, providing a sharp contrast against the more weakly varying scattering background.

To validate that the observed changes in the X-ray attenuation originate from the formation of the UiO-66 phase − and to demonstrate the capability of this approach to track the emergence of new crystalline phases − UiO-66 crystallization was independently studied by in situ time-resolved X-ray diffraction (XRD). Figure 2A shows the temporal evolution of X-ray diffractograms, revealing the progressive appearance and growth of Bragg reflections characteristic of UiO-66, with the most intense (111) and (002) diffraction peaks located at 2Θ values of 2.35° and 2.71°, respectively. The extent of solid formation, calculated from the integrated intensity of these two peaks and plotted as a function of crystallization time in Figure 2B, exhibits a sigmoidal profile similar to extent of solid formation calculated from X-ray attenuation, however, they are not perfectly coincident. These two metrics can differ because they reflect distinct physical observables. X-ray absorption is sensitive to the total number of Zr atoms in the beam path, irrespective of its degree of crystallinity, whereas XRD probes only coherently ordered domains that contribute to Bragg diffraction. As a result, attenuation can track changes in Zr density associated with the formation of amorphous or weakly ordered intermediates that do not yet contribute significantly to diffraction. In addition, Bragg intensities depend not only on the amount of crystalline material, but also on crystallite size, coherence length, structural disorder, and interference effects,[43] and therefore do not, a priori, scale strictly linearly with volumetric phase fraction during nucleation and growth. Minor differences between the datasets may also arise from the fact that XAS and XRD measurements were performed in separate experiments, where small variations in temperature or synthesis conditions cannot be fully excluded. Nevertheless, the metrics evaluated from X-ray diffraction and from X-ray attenuation exhibit an identical induction period of 25 min and closely similar kinetic trends. This agreement indicates that attenuation changes are

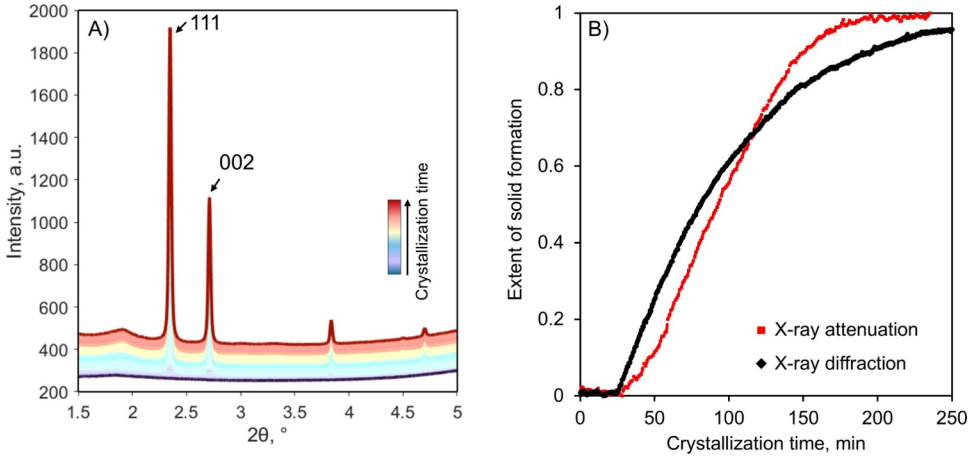

Figure 2. (A) Time-resolved XRD data acquired during the synthesis of UiO-66 at 363 K. XRD patterns are offset for visual purposes. (B) The extent of solid formation during UiO-66 synthesis at 363 K calculated from XRD data (black diamonds) and X-ray attenuation in post-edge region using eq 1 (red squares).

https://doi.org/10.1021/acsmaterialslett.6c00237
ACS Materials Lett. 2026, 8, 1974−1981

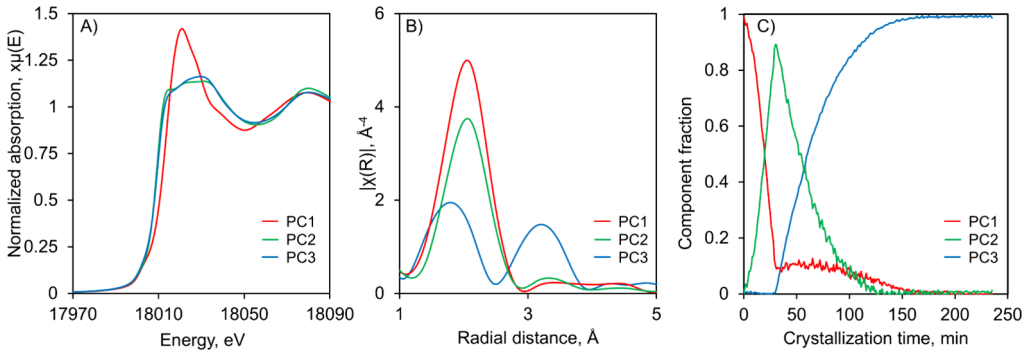

Figure 3. The results of the MCR-ALS analysis of the Zr K-edge time-resolved datasets of UiO-66 synthesis: XANES (A) and FT EXAFS (B) spectra corresponding to PC1, PC2, and PC3 and the temporal evolution of the different components during the crystallization at 363 K (C).

predominantly governed by resonant Zr absorption and that scattering contributions remain secondary. Consequently, X-ray attenuation provides a robust and sensitive tool for monitoring the kinetics of phase transformations, complementary to diffraction-based measurements.

Notably, this approach requires no additional data acquisition and can be readily applied to any well-collected transmission, and, potentially, fluorescent XAS dataset. As all XAS measurements are obtained within a single experiment, the temporal evolution observed in XANES and EXAFS can be directly correlated with crystallization kinetics extracted from the X-ray attenuation. This integration circumvents potential discrepancies arising from differences in experimental conditions when comparing independently collected XAS and XRD data, typically coming from different beamlines. We demonstrate the versatility of this method by applying it to monitor the crystallization of the UiO-66 MOF.

First, conventional Zr K-edge XANES and Fourier-transformed (FT) EXAFS spectra collected during UiO-66 crystallization were analyzed. The time-resolved, normalized XAS datasets were deconvoluted into linearly independent spectral components using multivariate curve resolution-alternating least squares (MCR-ALS) analysis.[44,45] Three linearly independent components are required to describe the evolution of the XAS spectra during UiO-66 crystallization (Figure 3A), denoted as Principal Components 1, 2, and 3 (PC1, PC2, and PC3, respectively), consistent with previous reports (Figures S3 and S4, Supporting Information).[19,20] The Zr K-edge FT EXAFS spectrum of PC1 features a single intense peak at approximately 2 Å radial distance (not phase-corrected), characteristic of zirconium chloroterephthalate species.[20] As synthesis progresses, PC1 gradually transforms into PC2 (Figure 4C), accompanied by a reduction in the intensity of the FT EXAFS peak reflecting the substitution of chloride ligands by oxygen atoms. PC2 is attributed to hydrolyzed zirconium-oxo complexes, including monomeric and oligomeric intermediates formed during hydrolysis. With further crystallization time, PC2 transitions into PC3. The Zr K-edge XANES and EXAFS spectra of PC3 closely resemble those of UiO-66, indicating that PC3 corresponds to $[Zr_6O_4(OH)_4]$ clusters structurally identical to the secondary building units (SBUs) of the UiO-66 metal–organic framework (Figure S2). Notably, the PC3 spectra obtained at different synthesis temperatures are indistinguishable (Figures S5 and S6, Table S1, Supporting Information), indicating that the local structure of the formed UiO-66 is invariant with temperature.

Since the PC3 component corresponds to the secondary building units (SBUs) of the UiO-66 crystal structure, its temporal evolution was compared to the kinetics of UiO-66 phase formation determined from the X-ray attenuation. Figure 4A,B show the extent of solid formation, as determined from the X-ray attenuation and the fraction of PC3, respectively, at different temperatures. All profiles exhibit a characteristic S-shaped curve with an induction period. These profiles are indicative of a two-stage crystallization mechanism involving distinct nucleation and crystal growth processes.

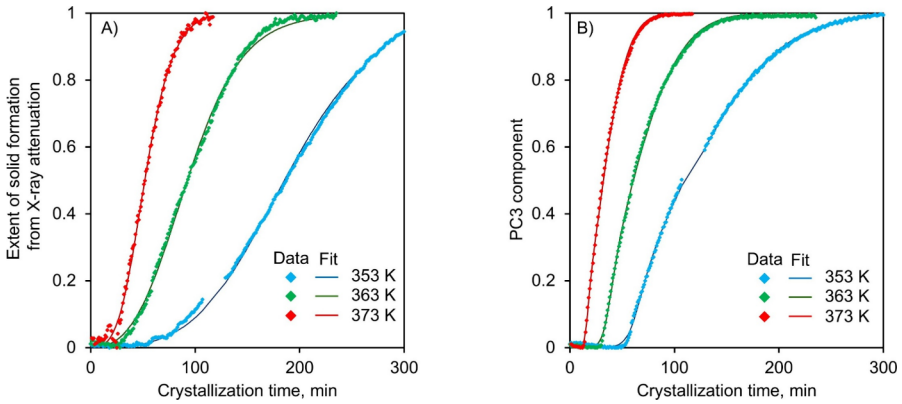

Figure 4. (A) Temporal evolution of the extent of solid formation for UiO-66 crystallization at different temperatures calculated from the X-ray attenuation using eq 1 and (B) the fraction of the PC3 component. Solid lines represent fits using the Gualtieri crystallization model (eq 2).

https://doi.org/10.1021/acsmaterialslett.6c00237
ACS Materials Lett. 2026, 8, 1974−1981

Table 1. Optimized Kinetic Parameters Obtained from Fitting the Extent of Solid Formation as a Function of Reaction Time Using the Gualtieri Model for UiO-66 Synthesis[a]

	X-ray attenuation data			PC3 temporal evolution		
sample parameter	353 K	363 K	373 K	353 K	363 K	373 K
$k_{growth}\cdot10^3$, min^{-1}	6.2(4)	13.3(9)	19.2(13)	7.9(5)	13.8(10)	26.8(15)
$k_{nucleation}\cdot10^3$, min^{-1}	6.7(4)	15.7(9)	29.8(15)	16(1)	27(2)	67(3)

[a]Parameters were determined based on the X-ray attenuation and the temporal evolution of the PC3 component.

For UiO-66 synthesized from zirconium tetrachloride and terephthalic acid in DMF with water and HCl as modulators, nucleation corresponds to the hydrolysis of zirconium chloride and zirconium chloroterephthalate complexes into zirconium–oxo species. The subsequent crystal growth step involves the condensation of monomeric and oligomeric zirconium–oxo complexes into SBUs with the $[Zr_6O_4(OH)_4]$ structure characteristic of UiO-66 and their assembling with terephthalate linkers from the solution. To quantitatively describe the crystallization kinetics, the Gualtieri model[46] was applied, allowing extraction of kinetic parameters associated with both nucleation and growth stages. According to this model, the time-dependent evolution of extent of solid formation, α, is expressed as:

$$\alpha = \frac{1}{1+e^{-\frac{t-a}{b}}}\left(1-e^{-(k_{growth}\bullet t)^n}\right) \quad (2)$$

where t represents the reaction time, k_{growth} is the rate constant for crystal growth, a is the reciprocal of the nucleation rate constant ($k_{nucleation}=\frac{1}{a}$), b reflects the variance in the nucleation probability distribution, and n corresponds to the dimensionality of the crystal growth process. The model accurately captures the observed crystallization kinetics, with fitted curves shown in Figure 4 closely matching the experimental data. The best-fit kinetic parameters are summarized in Table 1.

A comparison of kinetic parameters determined from the X-ray attenuation and the PC3 fractions reveals several noteworthy observations (Figure 5, Table 1). Crystal growth rate constants obtained from both methods are in close agreement across all reaction temperatures (Figure 5A). In contrast, the nucleation rate constants derived from the PC3 fraction are approximately two times higher than those obtained from X-ray attenuation (Figure 5B). This discrepancy arises because the two techniques probe different stages of structural evolution and, effectively, the formation of different detectable products.

The formation of PC3 species corresponds to the assembly of monomeric zirconium–oxo species into $[Zr_6O_4(OH)_4]$ nodes[19,20] and thus reflects the formation of SBUs at the molecular or unit-cell level. These species can be detected even when present as small and weakly ordered clusters. In contrast, changes in X-ray attenuation require the arrangement of clusters with linkers in quantities that induces sufficiently different density along the beam path, which occurs only after a critical extent of UiO-66 phase synthesis process has been achieved. As a result, attenuation responds to a later stage of the transformation, when clusters have assembled into larger, spatially extended domains. This difference introduces an effective detection threshold in attenuation-based metrics, such that the emergence of the new phase is observed only after a sufficient amount of organized material has formed. Consequently, the profile for the extent of solid formation derived from X-ray attenuation appears temporally delayed relative to PC3 evolution (Figure S7, Supporting Information) and more closely aligns with traditional XRD results (Figure 2B). Importantly, the crystal growth kinetics are captured similarly by both PC3 evolution and X-ray attenuation, leading to nearly identical crystal growth rate constants because crystal growth reflects the rate of new phase accumulation once nuclei are already formed.

Despite the differences in absolute rate constants for nucleation growth, Arrhenius analysis shows agreement between apparent activation energies obtained by two methods: both yield identical activation energies for nucleation (80 ± 7 kJ·mol^{-1}) and for crystal growth (64 ± 5 kJ·mol^{-1}), within experimental uncertainty. Notably, reported activation energies are close to those reported for UiO-66 synthesis earlier[19] or for Zr-fum MOF, where the same $[Zr_6O_4(OH)_4]$ nodes make up the SBU.[47]

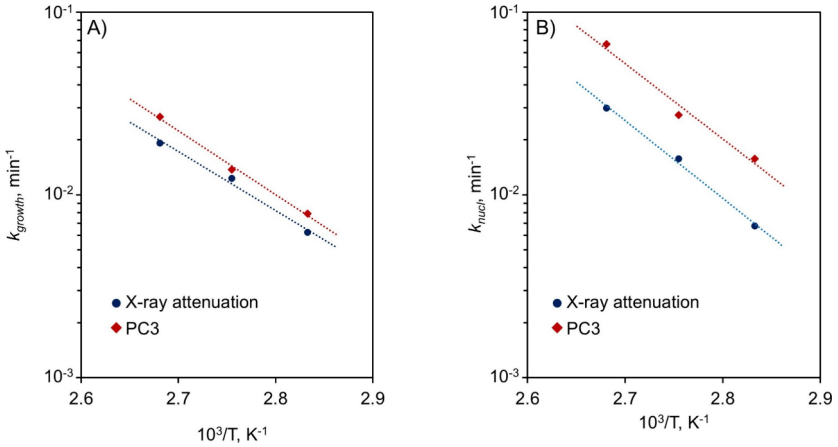

Figure 5. Arrhenius plots for crystal growth (A) and nucleation (B) rate constants extracted from the X-ray attenuation (blue circles) and PC3 temporal evolution (red diamonds) data using the Gualtieri model fit. Dotted lines show exponential regressions.

https://doi.org/10.1021/acsmaterialslett.6c00237
ACS Materials Lett. 2026, 8, 1974–1981

4. CONCLUSIONS

In conclusion, we show that quantification of the X-ray attenuation provides a powerful approach for tracking macroscopic phase transformations, including but not limited to crystallization, using standard transmission XAS data. This method requires no additional data acquisition and can be applied retroactively to any properly collected dataset. For a single-phase transformation occurring within a constant probed sample volume and under conditions where X-ray absorption dominates over elastic scattering, changes in X-ray attenuation directly reflect the extent of phase transformation and therefore complement conventional XANES and EXAFS analyses that focus on local atomic structure. Importantly, it serves as a functional analogue to XRD for detecting crystallization, with the key advantage of being acquired under identical experimental conditions, eliminating inconsistencies associated with separate measurements and potentially being applicable to the formation of non-crystalline phases. Applied to the crystallization of the UiO-66 metal−organic framework, this approach reliably captured both chemical and structural transformations, opening new possibilities for in situ characterization of dynamic material processes.

■ ASSOCIATED CONTENT

Supporting Information

The Supporting Information is available free of charge at https://pubs.acs.org/doi/10.1021/acsmaterialslett.6c00237.

Mathematical description of change in X-ray attenuation in systems with phase transformations and derivation of eq 1, comparison spectra of reference Zr compounds and MCR-ALS spectra obtained from analysis of XAS spectra during UiO-66 crystallization, comparison of temporal evolution of the fraction of the PC3 component, and the extent of solid formation for UiO-66 crystallization at different temperatures calculated from the X-ray attenuation (DOCX)

■ AUTHOR INFORMATION

Corresponding Author

Vitaly L. Sushkevich – *Center for Energy and Environmental Sciences, Paul Scherrer Institute, Villigen PSI 5232, Switzerland*; orcid.org/0000-0002-3788-8969; Email: vitaly.sushkevich@psi.ch

Authors

Mikalai A. Artsiusheuski – *Laboratory for the Science and Applications of Catalysis, Department of Chemical and Biomolecular Engineering, University of California at Berkeley, 275 Tan Hall, Berkeley, California 94720, United States*; orcid.org/0000-0003-4931-9568

Adam H. Clark – *Paul Scherrer Institute, Center for Photon Science, Villigen PSI 5232, Switzerland*; orcid.org/0000-0002-5478-9639

Maarten Nachtegaal – *Paul Scherrer Institute, Center for Photon Science, Villigen PSI 5232, Switzerland; Laboratory for Inorganic Chemistry, ETH Zurich, Vladimir-Prelog-Weg 1, Zurich 8093, Switzerland*; orcid.org/0000-0003-1895-9626

Nicola P. M. Casati – *Paul Scherrer Institute, Center for Photon Science, Villigen PSI 5232, Switzerland*; orcid.org/0000-0002-4206-9239

Jeroen A. van Bokhoven – *Institute for Chemistry and Bioengineering, ETH Zurich, Vladimir-Prelog-Weg 1, Zurich 8093, Switzerland; Center for Energy and Environmental Sciences, Paul Scherrer Institute, Villigen PSI 5232, Switzerland*; orcid.org/0000-0002-4166-2284

Complete contact information is available at: https://pubs.acs.org/doi/10.1021/acsmaterialslett.6c00237

Notes

The authors declare no competing financial interest.

■ ACKNOWLEDGMENTS

V.L.S. thanks the SNF for financial support, a part of this work was performed within Spark project CRSK-2_227415.

■ REFERENCES

(1) Feng, S.; Xu, R. New Materials in Hydrothermal Synthesis. *Acc. Chem. Res.* **2000**, *34* (3), 239–247.

(2) Cheetham, A. K.; Seshadri, R.; Wudl, F. Chemical Synthesis and Materials Discovery. *Nat. Synth.* **2022**, *1* (7), 514–520.

(3) Thanh, N. T. K.; Maclean, N.; Mahiddine, S. Mechanisms of Nucleation and Growth of Nanoparticles in Solution. *Chem. Rev.* **2014**, *114* (15), 7610–7630.

(4) Lee, J.; Yang, J.; Kwon, S. G.; Hyeon, T. Nonclassical Nucleation and Growth of Inorganic Nanoparticles. *Nat. Rev. Mater.* **2016**, *1* (8), 1–16.

(5) Cundy, C. S.; Cox, P. A. The Hydrothermal Synthesis of Zeolites: History and Development from the Earliest Days to the Present Time. *Chem. Rev.* **2003**, *103* (3), 663–701.

(6) Stock, N.; Biswas, S. Synthesis of Metal-Organic Frameworks (MOFs): Routes to Various MOF Topologies, Morphologies, and Composites. *Chem. Rev.* **2011**, *112* (2), 933–969.

(7) Baumgartner, B.; Wach, A.; Ye, X.; Ploetz, E.; Weckhuysen, B. M. Advancements in Understanding the Physicochemical Properties of Reticular Materials: An In Situ and Operando Spectroscopic Perspective. *Adv. Mater.* **2025**, *37* (52), No. 2415135.

(8) Achenbach, B.; Verel, R.; van Bokhoven, J. A.; Stock, N.; Sushkevich, V. L. Role of a Modulator in the Synthesis of an MIL-53 Metal−Organic Framework Revealed by In Situ Time-Resolved MAS NMR Spectroscopy. *J. Am. Chem. Soc.* **2025**, *147*, 44262.

(9) Wang, R.; Lu, K. Q.; Tang, Z. R.; Xu, Y. J. Recent Progress in Carbon Quantum Dots: Synthesis, Properties and Applications in Photocatalysis. *J. Mater. Chem. A* **2017**, *5* (8), 3717–3734.

(10) Karthika, S.; Radhakrishnan, T. K.; Kalaichelvi, P. A Review of Classical and Nonclassical Nucleation Theories. *Cryst. Growth Des.* **2016**, *16* (11), 6663–6681.

(11) Pienack, N.; Bensch, W.; Bensch, W.; Pienack, N. In-Situ Monitoring of the Formation of Crystalline Solids. *Angew. Chem., Int. Ed.* **2011**, *50* (9), 2014–2034.

(12) Li, J.; Deepak, F. L. In Situ Kinetic Observations on Crystal Nucleation and Growth. *Chem. Rev.* **2022**, *122* (23), 16911–16982.

(13) Salionov, D.; Semivrazhskaya, O. O.; Casati, N. P. M.; Ranocchiari, M.; Bjelić, S.; Verel, R.; van Bokhoven, J. A.; Sushkevich, V. L. Unraveling the Molecular Mechanism of MIL-53(Al) Crystallization. *Nat. Commun.* **2022**, *13* (1), 1–9.

(14) Norby, P. In-Situ XRD as a Tool to Understanding Zeolite Crystallization. *Curr. Opin. Colloid Interface Sci.* **2006**, *11* (2–3), 118–125.

(15) Wilkinson, A. P.; Speck, J. S.; Cheetham, A. K.; Natarajan, S.; Thomas, J. M. In Situ X-Ray Diffraction Study of Crystallization Kinetics in PbZr1-XTixO3, (PZT, x = 0.0, 0.55, 10). *Chem. Mater.* **2002**, *6* (6), 750–754.

(16) Kirsch, B. L.; Richman, E. K.; Riley, A. E.; Tolbert, S. H. In-Situ X-Ray Diffraction Study of the Crystallization Kinetics of Mesoporous Titania Films. *J. Phys. Chem. B.* **2004**, *108* (34), 12698–12706.
(17) Millange, F.; Medina, M. I.; Guillou, N.; FØrey, G. ø.; Golden, K. M.; Walton, R. I.; Golden, K. M.; Walton, R. I. Time-Resolved In Situ Diffraction Study of the Solvothermal Crystallization of Some Prototypical Metal−Organic Frameworks. *Angew. Chem.* **2010**, *122* (4), 775–778.
(18) Ragon, F.; Horcajada, P.; Chevreau, H.; Hwang, Y. K.; Lee, U. H.; Miller, S. R.; Devic, T.; Chang, J. S.; Serre, C. In Situ Energy-Dispersive x-Ray Diffraction for the Synthesis Optimization and Scale-up of the Porous Zirconium Terephthalate UiO-66. *Inorg. Chem.* **2014**, *53* (5), 2491–2500.
(19) Semivrazhskaya, O. O.; Salionov, D.; Clark, A. H.; Casati, N. P. M.; Nachtegaal, M.; Ranocchiari, M.; Bjelić, S.; Verel, R.; van Bokhoven, J. A.; Sushkevich, V. L. Deciphering the Mechanism of Crystallization of UiO-66 Metal-Organic Framework. *Small* **2023**, *19* (52), No. 2305771.
(20) Artsiusheuski, M. A.; Casati, N. P. M.; Clark, A. H.; Nachtegaal, M.; Verel, R.; van Bokhoven, J. A.; Sushkevich, V. L. Controlling the Mechanism of Nucleation and Growth Enables Synthesis of UiO-66 Metal−Organic Framework with Desired Macroscopic Properties. *Angew. Chem.* **2024**, *64* (4), No. e202415919.
(21) Kochetygov, I.; Maggiulli, L.; Ranocchiari, M.; Ferri, D. The Mechanism of Rapid and Green Metal−Organic Framework Synthesis by In Situ Spectroscopy and Diffraction. *Chem. Mater.* **2024**, *36* (14), 6877–6887.
(22) Embrechts, H.; Kriesten, M.; Hoffmann, K.; Peukert, W.; Hartmann, M.; Distaso, M. Elucidation of the Formation Mechanism of Metal−Organic Frameworks via in-Situ Raman and FTIR Spectroscopy under Solvothermal Conditions. *J. Phys. Chem. C* **2018**, *122* (23), 12267–12278.
(23) Petersen, T. D.; Balakrishnan, G.; Weeks, C. L. MOF Crystal Growth: UV Resonance Raman Investigation of Metal−Ligand Binding in Solution and Accelerated Crystal Growth Methods. *Dalton Trans.* **2015**, *44* (28), 12824–12831.
(24) Woerner, W. R.; Plonka, A. M.; Chen, X.; Banerjee, D.; Thallapally, P. K.; Parise, J. B. Simultaneous in Situ X-Ray Diffraction and Calorimetric Studies as a Tool To Evaluate Gas Adsorption in Microporous Materials. *J. Phys. Chem. C* **2015**, *120* (1), 360–369.
(25) Gaur, A.; Shrivastava, B. D. Speciation Using X-Ray Absorption Fine Structure (XAFS). *Rev. J. Chem.* **2015**, *5* (4), 361–398.
(26) Calvin, S. Ed., *XAFS for Everyone*; CRC Press: **2013**.
(27) Artsiusheuski, M. A.; Safonova, O.; Palagin, D.; van Bokhoven, J. A.; Sushkevich, V. L. Structural Evolution of Copper-Oxo Sites in Zeolites upon the Reaction with Methane Investigated by Means of Cu K-Edge X-Ray Absorption Spectroscopy. *J. Phys. Chem. C* **2023**, *127* (20), 9603–9615.
(28) Whitehead, C. B.; Finke, R. G. Particle formation mechanisms supported by in situ synchrotron XAFS and SAXS studies: A review of metal, metal-oxide, semiconductor and selected other nanoparticle formation reactions. *Mater. Adv.* **2021**, *2*, 6532–6568.
(29) Sankar, G.; Thomas, J. M. In Situ Combined X-Ray Absorption Spectroscopic and X-Ray Diffractometric Studies of Solid Catalysts. *Top. Catal.* **1999**, *8* (1−2), 1–21.
(30) Beale, A. M.; Reilly, L. M.; Sankar, G. Watching the Crystallisation of Complex Oxides by in Situ X-Ray Techniques. *Appl. Catal., A* **2007**, *325* (2), 290–295.
(31) Nonaka, T.; Dohmae, K.; Hayashi, Y.; Araki, T.; Yamaguchi, S.; Nagai, Y.; Hirose, Y.; Tanaka, T.; Kitamura, H.; Uruga, T.; Yamazaki, H.; Yumoto, H.; Ohashi, H.; Goto, S. Toyota Beamline (BL33XU) at SPring-8. *AIP Conf. Proc.* **2016**, *1741* (1), No. 030043.
(32) DIFFABS French national synchrotron facility. https://www.synchrotron-soleil.fr/en/beamlines/diffabs (accessed 2025-10-12).
(33) B18 End Station - - Diamond Light Source. https://www.diamond.ac.uk/Instruments/Spectroscopy/B18/Station.html (accessed 2025-10-12).
(34) BM31. https://www.esrf.fr/UsersAndScience/Experiments/CRG/BM01/bm01b (accessed 2025-10-12).
(35) Bornmann, B.; Kläs, J.; Müller, O.; Lützenkirchen-Hecht, D.; Frahm, R. The Quick EXAFS Setup at Beamline P64 at PETRA III for up to 200 Spectra per Second. *AIP Conf. Proc.* **2019**, *2054* (1), No. 040008.
(36) Henke, B. L.; Gullikson, E. M.; Davis, J. C. X-Ray Interactions: Photoabsorption, Scattering, Transmission, and Reflection at E = 50–30, 000 EV, Z = 1-92. *At. Data Nucl. Data Tables* **1993**, *54*, 181–342.
(37) Akbulut Özen, S.; Özen, M.; Şahin, M.; Mertens, M. Study of the Hydrothermal Crystallization Process of Barium Titanate by Means of X-Ray Mass Attenuation Coefficient Measurements at an Energy of 5954 KeV. *Mater. Charact.* **2017**, *129*, 329–335.
(38) Lomachenko, K. A.; Molokova, A. Y.; Atzori, C.; Mathon, O. Quantification of Adsorbates by X-Ray Absorption Spectroscopy: Getting TGA-like Information for Free. *J. Phys. Chem. C* **2022**, *126* (11), 5175–5179.
(39) Müller, O.; Nachtegaal, M.; Just, J.; Lützenkirchen-Hecht, D.; Frahm, R. Quick-EXAFS Setup at the SuperXAS Beamline for in Situ X-Ray Absorption Spectroscopy with 10 Ms Time Resolution. *Synchrotron Radiat.* **2016**, *23* (1), 260–266.
(40) Clark, A. H.; Imbao, J.; Frahm, R.; Nachtegaal, M. ProQEXAFS: A Highly Optimized Parallelized Rapid Processing Software for QEXAFS Data. *J. Synchrotron Radiat.* **2020**, *27* (2), 551–557.
(41) Patterson, B. D.; Abela, R.; Auderset, H.; Chen, Q.; Fauth, F.; Gozzo, F.; Ingold, G.; Kühne, H.; Lange, M.; Maden, D.; Meister, D.; Pattison, P.; Schmidt, T.; Schmitt, B.; Schulze-Briese, C.; Shi, M.; Stampanoni, M.; Willmott, P. R. The Materials Science Beamline at the Swiss Light Source: Design and Realization. *Nucl. Instruments Methods Phys. Res. Sect. A Accel. Spectrometers, Detect. Assoc. Equip.* **2005**, *540* (1), 42–67.
(42) Willmott, P. R.; Meister, D.; Leake, S. J.; Lange, M.; Bergamaschi, A.; Böge, M.; Calvi, M.; Cancellieri, C.; Casati, N.; Cervellino, A.; Chen, Q.; David, C.; Flechsig, U.; Gozzo, F.; Henrich, B.; Jäggi-Spielmann, S.; Jakob, B.; Kalichava, I.; Karvinen, P.; Krempasky, J.; Lüdeke, A.; Lüscher, R.; Maag, S.; Quitmann, C.; Reinle-Schmitt, M. L.; Schmidt, T.; Schmitt, B.; Streun, A.; Vartiainen, I.; Vitins, M.; Wang, X.; Wullschleger, R. The Materials Science Beamline Upgrade at the Swiss Light Source. *J. Synchrotron Radiat.* **2013**, *20* (5), 667–682.
(43) Magnussen, O. M.; Drnec, J.; Qiu, C.; Martens, I.; Huang, J. J.; Chattot, R.; Singer, A. In Situ and Operando X-Ray Scattering Methods in Electrochemistry and Electrocatalysis. *Chem. Rev.* **2024**, *124* (3), 629–721.
(44) Wasserman, S. R. The Analysis of Mixtures: Application of Principal Component Analysis to XAS Spectra. *J. Phys. IV JP* **1997**, *7* (C2), No. C2-203.
(45) Beauchemin, S.; Hesterberg, D.; Beauchemin, M. Principal Component Analysis Approach for Modeling Sulfur K-XANES Spectra of Humic Acids. *Soil Sci. Soc. Am. J.* **2002**, *66* (1), 83–91.
(46) Gualtieri, A. F. Synthesis of Sodium Zeolites from a Natural Halloysite. *Phys. Chem. Miner.* **2001**, *28* (10), 719–728.
(47) Zahn, G.; Zerner, P.; Lippke, J.; Kempf, F. L.; Lilienthal, S.; Schröder, C. A.; Schneider, A. M.; Behrens, P. Insight into the Mechanism of Modulated Syntheses: In Situ Synchrotron Diffraction Studies on the Formation of Zr-Fumarate MOF. *CrystEngComm* **2014**, *16* (39), 9198–9207.

https://doi.org/10.1021/acsmaterialslett.6c00237
ACS Materials Lett. 2026, 8, 1974−1981